Bacterial Stern layer diffusion: experimental determination with spectral induced polarization and sensitivity to nitrite toxicity

Adrian Mellage[1,2]*, Christina M. Smeaton[2], Alex Furman[3], Estella A. Atekwana[4], Fereidoun Rezanezhad[2] and Philippe Van Cappellen[2]

[1]*Center for Applied Geoscience, Hydrogeology, University of Tübingen, Tübingen, Germany,* [2]*Water Institute and Department of Earth and Environmental Sciences, University of Waterloo, Ontario, Canada,* [3]*Civil and Environmental Engineering, Technion – Israel Institute of Technology, Haifa, Israel, and* [4]*Department of Geological Sciences, College of Earth, Ocean, and Environment, University of Delaware, Newark, Delaware*

ABSTRACT

Spectral induced polarization signatures have been used as proxies for microbial abundance in subsurface environments, by taking advantage of the charged properties of microbial cell membranes. The method's applicability, however, remains qualitative, and signal interpretation ambiguous. The adoption of spectral induced polarization as a robust geo-microbiological tool for monitoring microbial dynamics in porous media requires the development of quantitative relationships between biogeochemical targets and spectral induced polarization parameters, such as biomass density and imaginary conductivity (σ''). Furthermore, deriving cell density information from electrical signals in porous media necessitates a detailed understanding of the nature of the cell membrane surface charge dynamics. We present results from a fully saturated sand-filled column reactor experiment where *Shewanella oneidensis* growth during nitrate reduction to ammonium was monitored using spectral induced polarization. While our results further confirm the direct dependence of σ'' on changing cell density, Cole–Cole derived relaxation times also record the changing surface charging properties of the cells, ascribed to toxic stress due to nitrite accumulation. Concurrent estimates of cell size yield the first measurement-derived estimation of the apparent surface ion diffusion coefficient for cells ($D_s = 5.4 \pm 1.3$ μm^2 s^{-1}), strengthening the link between spectral induced polarization and electrochemical cell polarization. Our analysis provides a theoretical framework on which to build σ''–cell density relations using bench-scale experiments, leading to eventual robust non-destructive monitoring of *in situ* microbial growth dynamics.

Key words: Induced Polarization, Environmental, Shallow Subsurface.

1 INTRODUCTION

Functional groups on bacterial cell membranes (Cox *et al.* 1999; Sokolov *et al.* 2001; Claessens, Behrends and Van Cappellen 2004) result in the development of a net negative surface charge at near-neutral pH, for both gram-positive and gram-negative bacteria (Revil *et al.* 2012). Because of this

surface charge, bacteria in contact with water are surrounded by an electrical double layer (EDL; Zhang *et al.* 2014). Spectral induced polarization (SIP) is an active geophysical method that measures electric conduction and charge storage, based on the difference in properties between injected and detected waveforms (see Kemna *et al.* 2012 for method details). Below 100 Hz, electrochemical polarization (i.e. the tangential migration of counterions when current is applied) within the

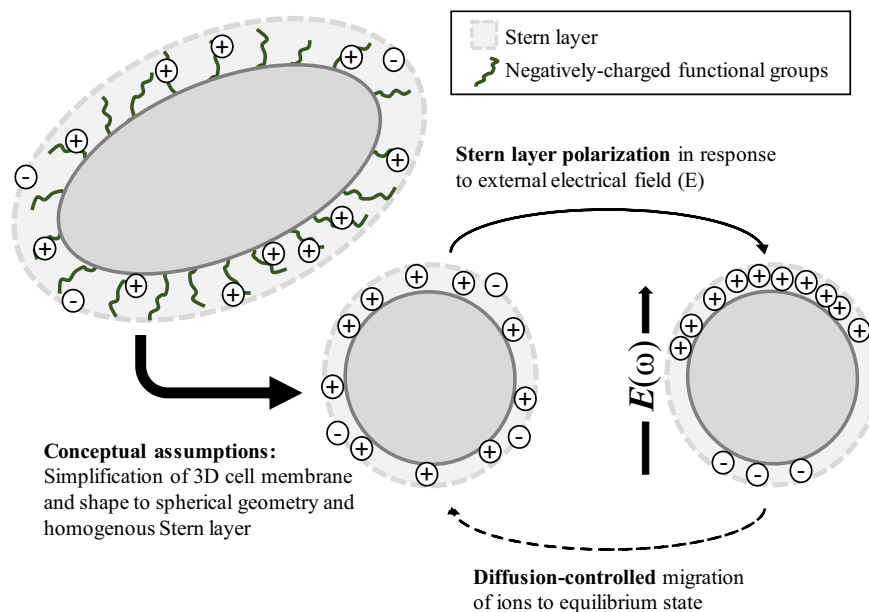*E-mail: adrian.mellage@uni-tuebingen.de

Figure 1 Conceptual diagram of Stern layer microbial cell polarization (partially modified from Mellage *et al.* 2018b), including the assumption that polarizing cells are of spherical geometry, and that charge migration within their three-dimensional (3D) outer cell membrane resembles that of adsorbed cations within the Stern layer of the EDL. Diffusion-controlled tangential migration of ions back to their equilibrium state can be described by the Schwarz (1962) model.

EDL of charged surfaces is responsible for the bulk of charge storage (Kemna *et al.* 2012). This is conceptualized in Fig. 1, for idealized Stern layer polarization within the EDL of cells.

Imaginary conductivity (σ''), the charge storage component of SIP, has been shown to exhibit a dependence on microbial abundance (Davis *et al.* 2006). Using suspensions of *Zymomonas mobilis*, Zhang *et al.* (2014) showed the dependence of σ'' on variable cell concentrations. These authors proposed a linear relationship between cell density and σ'', based on measurements performed at three cell concentrations. Mellage *et al.* (2018b) showed that time series σ'' peak values parallel the microbial growth and decay dynamics in a *Shewanella oneidensis* inoculated column experiment. These authors introduced a conceptual model in which charge storage is governed by the cell EDL, and where the time scale for ion back diffusion, as measured by the Cole–Cole relaxation time, τ, is a function of cell size and surface-charging properties of the cells.

Furthermore, studies focusing on the effect of biofilm formation on SIP signals (e.g. Abdel Aal, Atekwana and Atekwana 2010; Rosier *et al.* 2019), measured increasing σ'' with increasing cell density of *Pseudomonas aeruginosa*, in both flow-through columns and cell suspensions, respectively. Rosier *et al.* (2019) found that SIP signals from *P. aeruginosa*

suspensions varied in response to artificially added biofilm components (alginate, phenazine and DNA). Abdel Aal *et al.* (2010) suggested that a parallel contribution of increasing biomass and bioclogging contributed to increases in σ'' during microbial growth and biofilm formation.

While SIP signal changes are widely interpreted as a proxy for biogeochemical activity, the method's applicability remains qualitative, and signal interpretation ambiguous. There is a need for the development of quantitative relationships between biogeochemical targets and SIP parameters to derive, for example, cell densities from electrical signals in porous media. Such relationships would facilitate bench-scale, non-destructive monitoring of microbial dynamics.

In this study, we build on the work of Mellage *et al.* (2018b) and propose a quantitative relationship between cell density and σ'' for *S. oneidensis* in microbial growth quartz sand column incubations. Our analysis further sheds light on the mechanisms driving the observed relaxation time dynamics as a result of changes in microbial abundance and activity. Moreover, cell size measurements coupled to a model of charge relaxation within the Stern layer of the EDL (Schwarz 1962) are used to estimate the surface ion diffusion rates of polarizing cells. Our analysis further shows that relaxation time anomalies are linked to changes in microbial physiological state, here likely induced by nitrite (NO_2^-) toxicity.
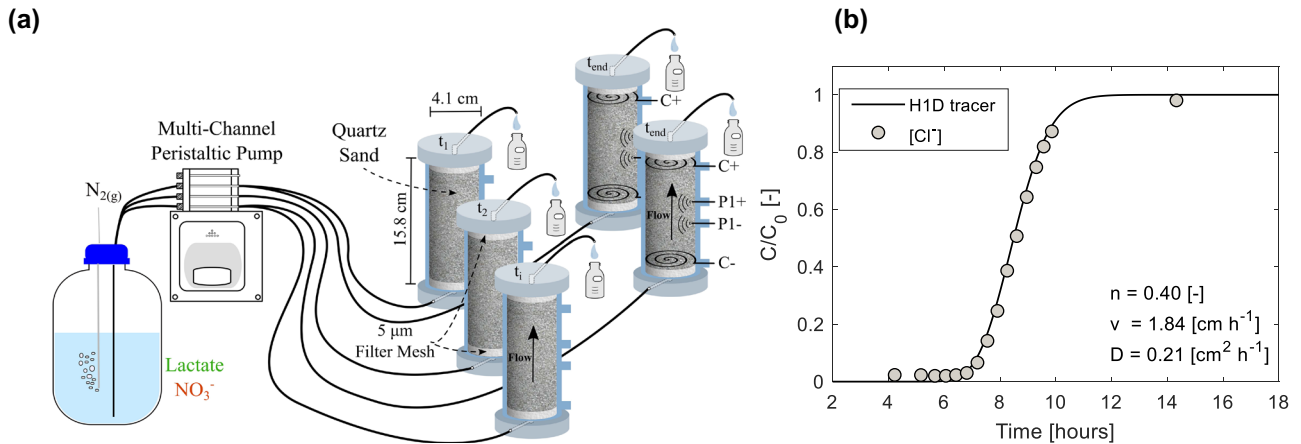
Figure 2 Schematic of the flow-through reactor set-up (a). The experiment consisted of 10 columns, 2 of which were fitted with the electrode array for SIP measurements. The other 8 columns were sacrificially sampled at specific times during the experiment. The two SIP columns were sampled at the end of the experiment. The normalized concentration (C/C_0) breakthrough curve (measured and fitted) for a continuous Cl⁻ tracer injection is shown in panel (b). Parameters (n = porosity, v = velocity and D = dispersion) extracted from the fitted numerical solution in Hydrus 1D (H1D) are also presented.

2 MATERIALS AND METHODS

2.1 Flow-through column reactors

The experiment was run in 10 identical high density polyethylene (HDPE) column reactors with an inner diameter of 4.1 cm, length of 15.8 cm (Fig. 2a), fitted with four lateral ports, allowing pore water and bulk sand sampling and, in the two columns fitted for spectral induced polarization (SIP) measurements (herein referred to as G1 and G2), electrode emplacement. In the eight (out of ten) replicates not fitted with SIP electrodes, ports were sealed with national-pipe-thread (NPT) compression fittings. Prior to column assembly, all experimental components, including the sand, were sterilized as described in Mellage *et al.* (2018b).

Columns were wet packed to a porosity of 40% (determined from a tracer breakthrough curve; Supporting Information Fig. S1) in an anaerobic chamber (Coy, < 1 ppmv O_2 in N_2 with 3% H_2) with sterile quartz sand (U.S. Silica, F-45, grain size range: 0.15–0.42 mm). A pH-buffered (pH = 7.5) microbial growth medium containing 10 mM lactate, 1.5 mM nitrate (NO_3^-) and 0.4 mM ammonium (NH_4^+) was used as the saturating pore solution and the inflow solution during injections (see Mellage *et al.* 2018b). An overnight aerobic culture of *S. oneidensis* MR1 was grown in Luria Bertani medium, harvested via centrifugation and inoculated into the growth medium. The growth medium was then used as the saturating pore solution to wet pack the columns, yielding a starting cell density of 8.3×10^4 cells mL_{PM}^{-1} (where mL_{PM} refers to the bulk volume of the porous medium, i.e.
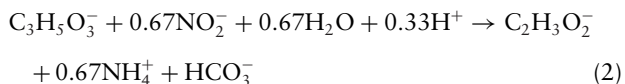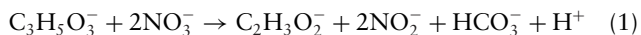
solid phase plus pore water). The columns were incubated for a total of 315 hours, following the first substrate injection (see details below).

Reactors were sealed with HDPE screw end-caps at either end, fitted with inflow and outflow channels at the bottom and top, respectively. Two filter membranes were placed at each end (0.2-µm polypropylene and 5-µm glass), to promote laminar flow conditions and minimize the loss of bacteria from the flow-through reactor system. Viton tubing (1/16″ i.d.; 1/8″ o.d.; 1/32″ wall, Cole-Parmer Instrument Company, Vernon Hills, IL, USA) was used to connect the columns to a peristaltic pump (Minipuls 3; Gilson, Middleton, WI, USA) for flow injection (Fig. 2a).

A continuous tracer injection (Cl⁻) was performed on a preliminary packed flow-through column (without electrodes, to avoid Cl⁻ contamination from the 1 M KCl) to determine the time to 50% tracer breakthrough (i.e. 1 pore volume). A 2.2 (±0.03) mM Cl⁻ containing solution was injected for 14.5 hours at an average flow rate of 9.84 (±0.52) mL h⁻¹. Chloride concentrations were measured in periodic outflow samples with a chloride-ion-selective electrode (Thermo Fisher Scientific, Beverly, MA, USA). Hydrus 1D was used to fit numerically solved advection–dispersion parameters (dispersion, $D = 0.21$ cm² h⁻¹; and velocity, $v = 1.84$ cm h⁻¹) to the measured Cl⁻ breakthrough (Simunek, Van Genuchten and Sejna 2005). From the fitted breakthrough curve in Fig. 2(b), it is evident that at 12 hours (1.4 pore volumes), the outflow concentration is equal to that at the inflow in our experimental set-up.

2.2 Microbial activity

Injections of lactate and NO_3^- were aimed to mimic the experimental conditions in Mellage *et al.* (2018b) and stimulate growth of *S. oneidensis*. During dissimilatory nitrate reduction to ammonium (DNRA), *S. oneidensis* oxidizes lactate to produce acetate, and NO_3^- is reduced to NH_4^+ via NO_2^- (Gao *et al.* 2009; Zhang *et al.* 2013):

$$C_3H_5O_3^- + 2NO_3^- \rightarrow C_2H_3O_2^- + 2NO_2^- + HCO_3^- + H^+ \quad (1)$$

$$C_3H_5O_3^- + 0.67NO_2^- + 0.67H_2O + 0.33H^+ \rightarrow C_2H_3O_2^- \\ + 0.67NH_4^+ + HCO_3^- \quad (2)$$

NO_2^-, the intermediate product, is toxic to *S. oneidensis* at concentrations higher than 1 mM (Zhang *et al.* 2013), and can inhibit both DNRA and biomass growth (Sijbesma *et al.* 1996). Conceptually, NO_3^- and lactate replenishment via two 12-hour injections supplies both energy and a carbon source and should result in growth, thereby resulting in higher σ'' magnitudes. However, the potential accumulation of NO_2^-, in excess of 1 mM, can result in inhibited microbial growth.

Following an initial no-flow pre-equilibration phase, inflow solution containing both lactate and NO_3^- was injected (t_0) for 12 hours at an average flow rate of 8.9 (± 1.0) mL h^{-1}, herein referred to as phase I. Inflow solution injection replaced the pore water in the columns and replenished the electron acceptor (NO_3^-) and electron donor/carbon source (lactate). Flow injection lasted for the minimum time-interval required to completely replace the pore volume of the columns (i.e. 12 hours), as confirmed by the chloride breakthrough tracer curve (Fig. 2b). After 12 hours, the flow was stopped; the columns were sealed and incubated under no-flow conditions for 155 hours, hereafter referred to as phase II. A second 12-hour injection (i.e. phase III) occurred at 167 hours at an average flow rate of 9.3 (± 0.5) mL h^{-1}. Following the second injection, the columns were incubated for 136 hours under no-flow conditions (phase IV). We chose to conduct a periodic-flow injection experiment to successfully replenish NO_3^- and lactate in the pore fluid. The no-flow incubation period was meant to minimize SIP signal contributions related to transport and microbial dynamics under transport conditions.

2.3 Pore water and bulk sand sampling and analysis

The first replicate column was sacrificially sampled prior to phase I, at t_0, followed by sequential sampling of the other columns at selected time points. Pore water samples (1 mL) were collected using ceramic samplers, 5 cm in length and 2.5 mm in diameter with a filter pore size of 0.15 μm (CSS5 MicroRhizon samplers, Ejikelamp, the Netherlands, #19.21.23F). Samples were analysed for lactate, acetate and NO_3^- using ion chromatography (Dionex ICS-5000, Ion-Pac AS18 column), and NO_2^- and NH_4^+ were analysed using microplate-based colorimetric methods (FlexStation 3, Molecular Devices, San Jose, CA, USA; Ringuet, Sassano and Johnson 2011).

To remove biomass from the sand for cell counting with flow cytometry, bulk sand samples (approximately 2 g) were collected from the ports at the centre of the columns (see Fig. 2) with a mini-auger, weighed, treated with 10 mL of a 10 mM Tris-HCl, 1 mM EDTA buffer solution (Tris-EDTA pH = 7.4; Sigma-Aldrich, Millipore Sigma Canada Co., Oakville, ON, Canada) containing 0.1% IGEPAL (IGEPAL CA-630, Sigma-Aldrich), and sonicated for 10 minutes (Neal *et al.* 2003). Adenosine triphosphate (ATP) content was determined through luminescence measurements using a cell viability assay kit (BacTiter-GloTM Microbial Cell Viability Assay). Enumeration and size estimation of total, unfixed cells was performed on a FACSaria Fusion flow cytometer (BD Biosciences). Cell size was determined at every sampling time point using non-fluorescent microbeads (flow cytometry size calibration kit, F-13838, Thermo Fisher). The relationship derived from the median forward scatter intensity (FSC-A) and the size of the different non-fluorescent microbeads (see Fig. S1 in the Supporting Information) was used to calculate the size of *S. oneidensis* cells using the median FSC-A of each cell density sample.

2.4 SIP measurements

Two of the 10 columns were fitted with non-polarizing, electrolyte-filled (1 M KCl, 15 g L^{-1} agar gel), Ag–AgCl potential electrodes encased in nylon 1/2" NPT compression fittings, and Ag–AgCl current coil electrodes (Fig. 2). Potential electrodes were placed in the centre of the columns (2.5 cm apart), and current electrodes were placed 4 cm from each potential electrode at either end of the column. A Portable Spectral Induced Polarization (PSIP) unit (Ontash & Ermac Inc., NJ, USA) was used to measure phase shift ($-\phi$) and conductivity magnitude ($|\sigma|$) over 51 log frequency steps

between 0.01 and 1000 Hz. (Note: for additional control measurements, please refer to Mellage *et al.* 2018b, where the same quartz sand and saturating pore solution were used and shown to have a negligible background polarization.)

The Cole–Cole relaxation model (Pelton *et al.* 1978) was fitted to measured SIP spectra (Weigand and Kemna 2016a,b), to extract relaxation times, according to the following equation:

$$\sigma^*(\omega) = \sigma_0 \left[1 + m \left(\frac{(i\omega\tau)^c}{1 + (i\omega\tau)^c (1-m)} \right) \right], \qquad (3)$$

where σ_0 [S m^{-1}] is the direct current conductivity, m [−] the chargeability, τ [s] the relaxation time, ω [rad s^{-1}] is the angular frequency, and c [−] is a constant describing the shape of the observed phase dispersion. As postulated by Mellage *et al.* (2018b), for signals dominated by electrochemical polarization of bacteria (conceptualized in Fig. 1), τ is a relative measure of the time for polarization and ion back diffusion as calculated by Schwarz (1962):

$$\tau = \frac{d^2}{8 D_s} \qquad (4)$$

Equation (4) implies that both the size of the polarizing bacteria (i.e. the effective diameter, d) and their surface charging properties (i.e. the surface diffusion coefficient, D_s) control the magnitude of τ.

3 RESULTS AND DISCUSSION

3.1 Spectral induced polarization: spectral response

Spectral σ'' responses for selected time points following the first and second injections are presented in Fig. 3. In the interest of conciseness, only the spectral results from spectral induced polarization (SIP) columns G2 are presented. (Note: a baseline comparison for spectra 10 hours prior to, and shortly after injection for both SIP columns, is presented in Supporting Information Fig. S2. Additionally, full temporal trends in peak-σ'' for G1 are shown in Fig. S3). Trends in SIP column G1 were similar to those in G2 during the first injection, but diverged during the second injection. This divergence between the columns was also observed in the measured cell density (Fig. S3), suggesting that the *S. oneidensis* cells displayed a higher mortality rate (i.e. decay), in column G1. The inter-column discrepancies are discussed in more detail in Section 3.3.

Following injections, σ'' decreased due to a flow-induced loss of cells, despite the presence of a filter membrane (pore size: 0.2 μm) at the outflow. This was substantiated by

measurements of cell counts in outflow samples on the order of $1(\pm 0.27) \times 10^4$ cells mL^{-1}, 2 hours after injection started, during both injection periods. Following the initial drop, σ'' increased and the spectra developed a distinct frequency peak between 4 and 8 Hz (Fig. 3a). Maximum σ'' (2.23×10^{-5} S m^{-1}) was reached following the second injection at 192 hours (Fig. 3b). The response decreased in magnitude by a factor of 2 during a 4-hour period, with an abrupt change in the location of the frequency peak from 4 to 0.2 Hz (195 hours in Fig. 3b). After the drop in response, σ'' began to recover and the peak shifted back to higher frequencies (Fig. 3c). The range of frequency peaks measured here falls within the range of peaks previously reported for *S. oneidensis* (Mellage *et al.* 2018b) and other bacterial strains (Zhang *et al.* 2014; Rosier *et al.* 2019).

3.2 Temporal trends: geochemistry

Time-series measurements of aqueous dissimilatory nitrate reduction to ammonium (DNRA) reactants and products, normalized peak-σ'' (for both SIP columns), τ for each SIP measurement (G2), and cell counts and size are presented in Fig. 4. Lactate and acetate concentrations are presented in Supporting Information Section S3 (see Fig. S4).

The different starting conditions, as a result of the preceding period (i.e. pre-equilibration phase versus following injection), resulted in slight variations in reaction kinetics between phases II and IV. Most notably, DNRA kinetics were slower after phase III than after phase I (Fig. 4a and b). At the end of phase I, the measured NO$_3^-$ concentration was 0.24 mM, implying that 84% of NO$_3^-$ was reduced during phase I, while NO$_2^-$ accumulated up to a value of 1.32 mM (Fig. 4b). Conversely, at the end of phase III, NO$_3^-$ accumulated to 1.34 mM (Fig. 4a), which translates to only 10% consumption, and NO$_2^-$ rose to 0.25 mM (Fig. 4b). At 195 hours, 28 hours after the onset of phase III, NO$_2^-$ had increased further to 0.65 mM, and NO$_3^-$ had dropped to 0.22 mM, suggesting that DNRA was still taking place. Depletion of both NO$_3^-$ and NO$_2^-$ was measured at 221 hours. During both phases I and III, NH$_4^+$ decreased to values close to the inflow concentration (0.4 mM), and increased during phases II and IV with the progression of DNRA to reach a maximum value of 1.54 and 1.6 mM, respectively.

Differences in DNRA kinetics can, in part, be a function of the activity of the bacteria, where despite the higher cell density and σ'', the number of active cells may have been lower during phase III. This is supported by the lower ATP concentrations (presented in Supporting Information Fig. S5),
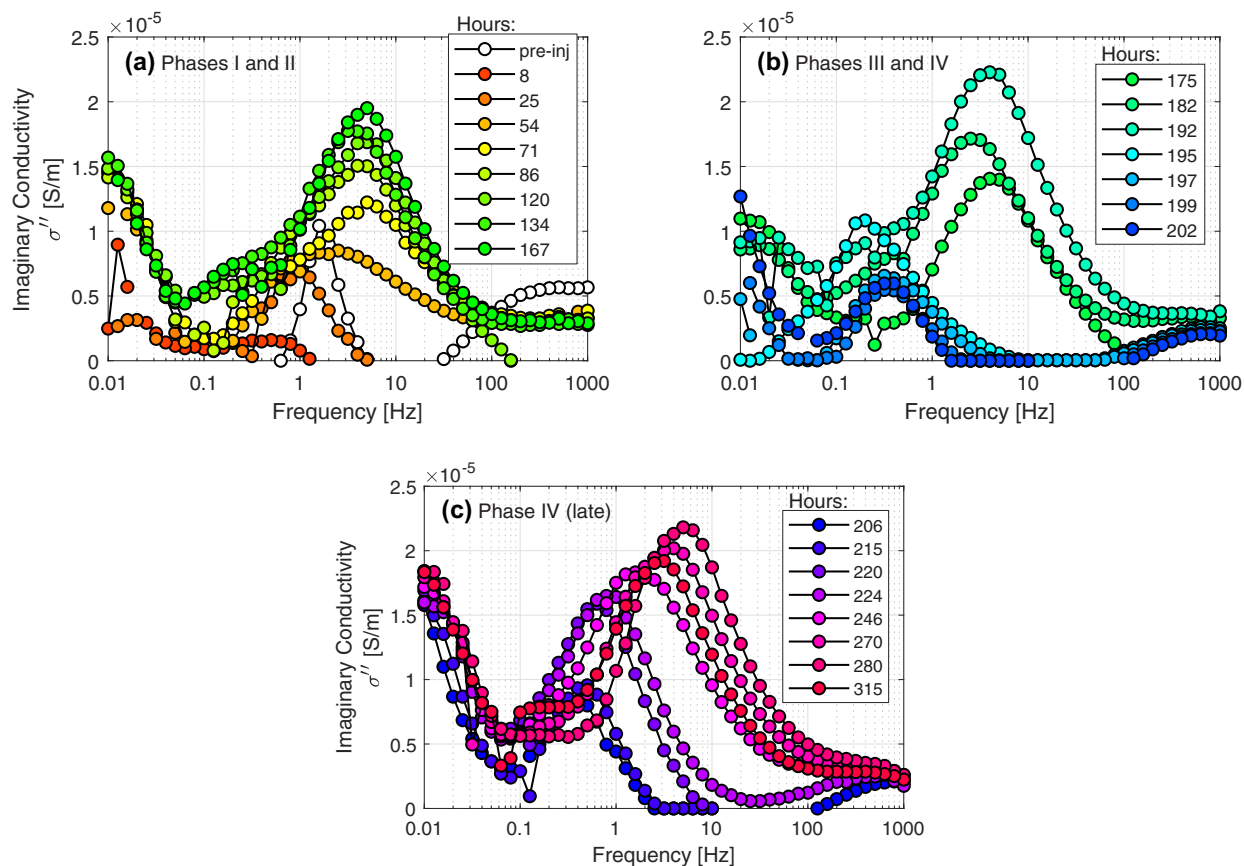
Figure 3 Spectral imaginary conductivity (σ'') results for selected time points 2 hours before lactate and NO_3^- injection (pre-inj), and following the first (a) and second injections (b) and (c), in SIP column G2. Legend entries correspond to incremental time points, in hours.

a proxy for microbial activity (Bastida *et al.* 2008), measured during phases III and IV.

The observed maximum NH_4^+ concentrations did not reach the expected value after complete DNRA, which would have been 1.9 mM (sum of NH_4^+ present in the media and produced by DNRA). About 0.05 mM of NH_4^+ would have been used by the bacteria as a nitrogen source to build microbial biomass (Russell and Cook 1995), estimated from the amount of biomass growth measured here, assuming an idealized biomass chemical composition of $C_5H_9O_{2.5}N$. The missing ~0.25 mM of NH_4^+ were likely bound in outer-sphere complexes at negatively charged sites on both the sand and cell membranes (Ceazan, Thurman and Smith 1989; Revil *et al.* 2012).

3.3 Temporal trends: SIP and biomass

Growth of *S. oneidensis* was stimulated following the injection of phase I, with increasing cell counts measured until the

end of phase III. Cell counts and normalized σ'' are plotted together in Fig. 4(c). The σ'' was normalized to remove slight differences in the measured magnitudes between columns G1 and G2 (see Supporting Information Fig. S2), which we ascribe to packing heterogeneities (e.g. Mellage *et al.* 2018a). Normalized σ'' was calculated as the difference between measured σ'', at a specific time, and σ'' immediately following the first injection (i.e. minimum at t_0), divided by the difference between the maximum and minimum (yielding a value between 0 and 1).

The biomass increase was matched by increasing σ'' signals in both SIP columns (G1 and G2). Cell counts for the column sacrificially sampled immediately before phase II are omitted, because propionate was detected, suggesting that the bacteria fermented lactate (Seeliger, Janssen and Schink, 2002), and that the column did not behave as a replicate. Temporal trends in peak-σ'' from a non-growth control column, inoculated with *S. oneidensis*, but devoid of NO_3^- and lactate, are compared with the SIP measurements in column G2
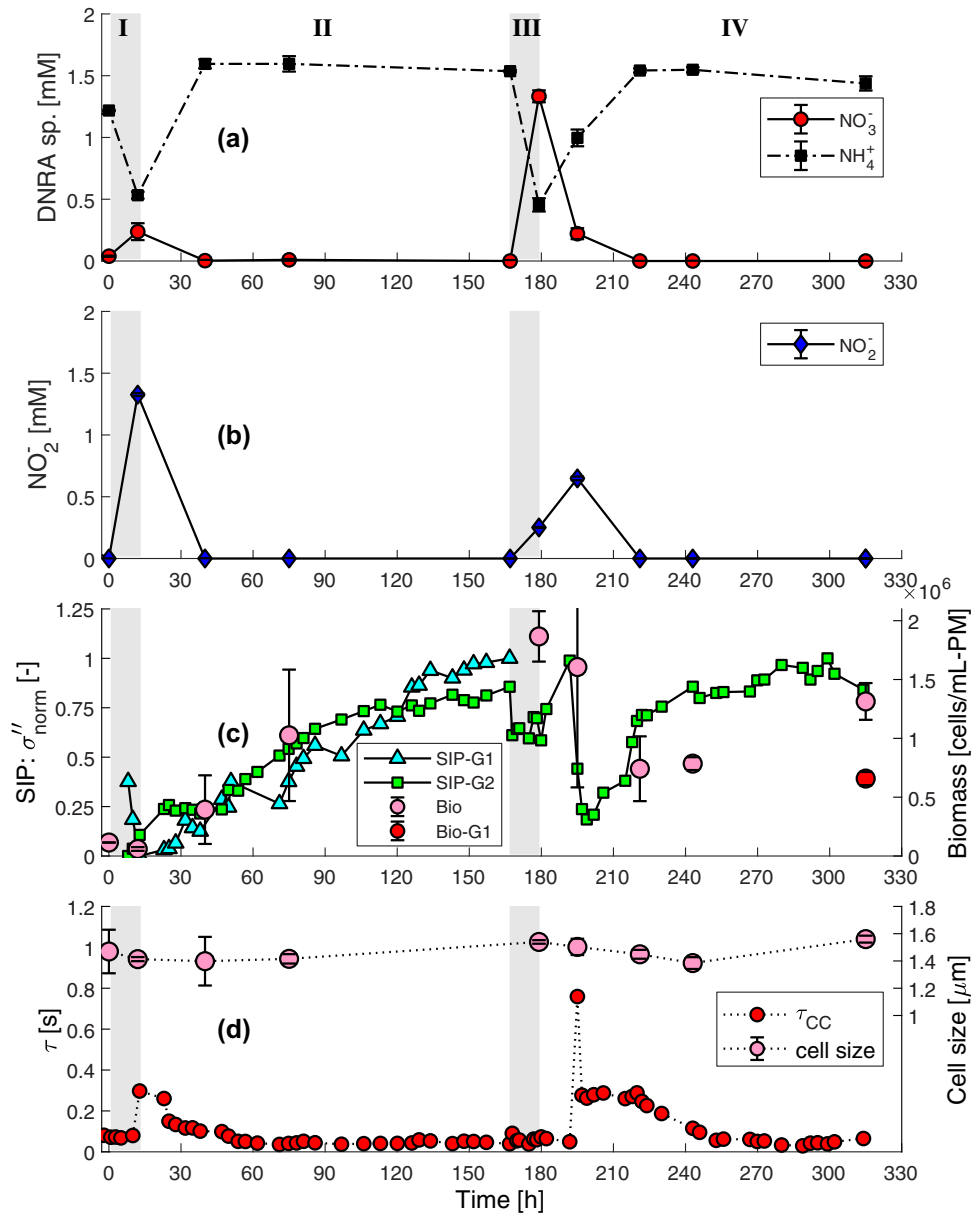
Figure 4 Dissimilatory nitrate reduction to ammonium (DNRA) species (NO_3^- and NH_4^+ (a), NO_2^- (b)) in each of the sacrificially sampled columns from the onset of lactate and NO_3^- injection. Biomass cell counts are compared with normalized imaginary conductivity (σ'') measured in duplicate (c) and cell size is compared with relaxation time (τ) dynamics (d). Grey bars represent injection periods. (Note: "Bio-G1" corresponds to the cell density measured in column G1, and the last measurement in the "Bio" time series corresponds to column G2.)

in Supporting Information Fig. S6. The absence of growth-stimulating conditions in the non-growth control is evident in the lower, and fairly constant, peak-σ'' signal throughout the incubation. These non-growth dynamics are consistent with those in a similar experiment by Mellage *et al.* (2018b), where measured σ'' magnitudes were constant, and consistently lower than biostimulated treatments.

Biomass density decreased following phase III (Fig. 4c) and increased only after 221 hours from 0.74×10^6 to 1.31×10^6 cells mL_{PM}^{-1}, at the end of incubation (315 hours). Peak-σ'' values dropped during phase III, but increased once injection had ceased reaching a maximum at 192 hours after which σ'' precipitously declined to a minimum by 199 hours. The decline in both cell density and peak-σ'' matched the timing of

NO_2^- accumulation (Fig. 4b). Following the drop, σ'' recovered gradually and increased until the end of the experiment, matching the increase in biomass.

Following the precipitous decline at 192 hours, σ'' in column G1 decreased continuously, and did not recover, which did not match the general trend in biomass and σ'' in G2 (refer to Fig. Supporting Information S3, after 192 hours). Both SIP columns G1 and G2 were sacrificially sampled in parallel, at the end of the incubation, $t = 315$ hours. Their cell densities were different by a factor of 2 (1.31×10^6 and 0.66×10^6 cells mL_{PM}^{-1}, for columns G2 and G1, respectively). (Note: 'Bio-G1' in Fig. 4c corresponds to the cell density measured in column G1, and the last measurement in the "Bio" time series corresponds to column G2). The discrepancy in cell densities matched the diverging trends in σ'' during phase IV, therefore, justifying the omission of σ'' in G1 during phases III and IV, from the general interpretation of the experimental results. The temporal dynamics in σ'' measured in G2 follow the unified trend measured across all biogeochemical markers more closely, and was therefore relied on for discussion of the overall data set and postulation of a quantitative relationship between SIP and biomass concentrations. Despite all reactors being prepared, to the best of our abilities, identically, the difference in trends in σ'' in the SIP columns, specifically after 215 hours (Supporting Information Fig. S3), suggests that the microbes in column G1 underwent higher decay thereafter, likely associated with NO_2^- inhibitory effects (Sijbesma *et al.* 1996; Zhang *et al.* 2013). We therefore rely on the overall trend in the geochemical data, and the SIP data set that best matches that behaviour, taking into account that each sampling point constituted a separate, sacrificially sampled flow-through reactor.

The matching trends of cell density and σ'' (Fig. 4c) provide direct experimental evidence for a correlation between SIP-σ'' and the electrochemical polarization of cells. The maximum magnitude of phase shift measured here was 0.6 mrad, for a maximum measured cell density of 1.87×10^6 cells mL_{PM}^{-1}, and a minimum of 0.09 mrad for a density of 5.97×10^4 cells mL_{PM}^{-1} (at the PSIP instrument detection limit). A linear relationship for estimating cell counts from peak-σ'' in quartz sand is presented in Fig. 5, giving the equation:

$$\text{Bio} = 1.46 \times 10^{11} \left(\sigma''\right) - 4.22 \times 10^5, \quad (5)$$

where Bio (cells mL_{PM}^{-1}) is the density of cells. The linear relationship in equation (5) is derived directly from cell counts measured using flow cytometry and peak-σ'' values in G2, prior to the precipitous drop in σ'' measured after 192 hours ($R^2 = 0.83$). The regression was performed only
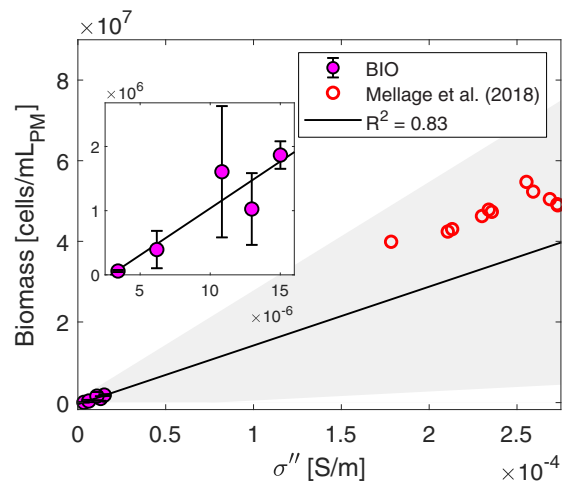

Figure 5 Linear relationship (equation (5)) between measured cell counts (FACS) and imaginary conductivity (σ'') ($R^2 = 0.83$), prior to the precipitous decline in σ'' at 195 hours (95% CI, grey shaded area). Mellage *et al.* (2018b) σ'' values, following 124 hours of incubation in quartz sand, fall close to the measurement-derived line.

on the time points prior to 195 hours, because of evidence suggesting strong changes in the cells' surface-charging properties thereafter, based on the measured τ dynamics (Mellage *et al.* 2018b).

Equation (5) predicts cell concentrations consistent with those simulated in a previous study (Mellage *et al.* 2018b) for the same cell strain and porous medium (Fig. 5). The data from Mellage *et al.* (2018b) fall close to, but not directly on, the line predicted by equation (5). The presence of elevated Fe^{2+} concentrations, stemming from the iron-coated sand in that experiment, could have, in part, contributed to the discrepancy. Furthermore, slight variations in reaction kinetics across the replicate columns could have resulted in an offset between the timing of changes in σ'', measured in the SIP columns, and concentration changes, measured in the sampled column.

The slope of equation (5) is two orders of magnitude lower than that between SIP measurements and cell densities reported in Zhang *et al.* (2014). The discrepancy between the relationship derived for *S. oneidensis* in non-polarizing quartz sand (see Mellage *et al.* 2018b) and *Z. mobilis* suspensions in Zhang *et al.* (2014) is likely a function of several factors in their experiments, including the different potential electrode construction (i.e. encased in electrolyte versus in direct contact with sample), different bacterial strains, the metabolic/physiological state of the cells (i.e. recently prepared suspension versus cells under growth conditions), and the

similar magnitude of the three cell densities in the regression analysis in Zhang *et al.* (2014). Future research must address these key factors with the goal of developing unified relationships for estimation of cell density from σ'' measurements. Nevertheless, the agreement between the data set presented here and that reported in Mellage *et al.* (2018b; see Fig. 5) provides confidence in the validity of the empirical relationship (equation (5)) and is promising for the development of SIP as an in-line monitoring technique for microbial growth dynamics.

Normalized chargeability (m_n) and τ values were extracted from the fit of a single Cole–Cole relaxation to SIP spectra from column G2 to obtain information for the frequency peak between 0.05 and 100 Hz. Cole–Cole parameters from column G1 are not presented due to the partial omission of that data set, and the less pronounced peak response (e.g. Fig. S2), yielding a less reliable fit. Examples of the goodness-of-fit at selected time points are presented in Fig. 6. Overall, a single Cole–Cole term fits both the early and late time spectra well (Fig. 6). At later times, the SIP response in the low frequency range slightly deviates from the predicted spectral shape (e.g. at 280 hours; Fig. 6d). Nevertheless, considering the overall fit to the entire data set, we determined that a single Cole–Cole term sufficiently captured the frequency dependence of the entire data set.

Time-series m_n dynamics are plotted along with cell density measurements in Fig. 7(a). A regression analogous to equation (5) (in Fig. 5), but comparing m_n and biomass density, is plotted in Fig. 7(b). In agreement with the σ'', m_n, also a measure of charge storage, exhibits a positive correlation with increasing cell density. Revil *et al.* (2012) proposed a linear equation describing the relationship between m_n and biomass density, where the slope is dependent on both petrophysical properties of the background medium (e.g. quartz sand) and microbial physiological and charging parameters:

$$m_n = \frac{2}{3}\left(\frac{\phi}{1-\phi}\right)m_B\left(\beta_{(+)}V_B\rho_B\mathrm{CEC}_B\right)\mathrm{Bio}. \qquad (6)$$

In equation (6) $m_B(-)$ is the Archie cementation exponent (Archie 1942), $\beta_{(+)}$ is the counter-ion mobility within the Stern layer (m^2 s^{-1} V^{-1}), V_B is the volume of one bacterium (m^3), ρ_B is the mass density of active bacteria (kg m^3), CEC_B is the cation exchange capacity of an active bacterial cell (C kg^{-1}), and Bio is the number of cells per unit bulk volume. Applying our measured m_n values, the parameters for bacterial cells outlined in Revil *et al.* (2012), and a CEC_B of 5 × 10^5 (C kg^{-1}), for *Shewanella* spp. (Chubar, Behrends and Van Cappellen 2008), we found that equation (6) overpredicts cell density by an order of magnitude (predicted biomass plots well outside the range in Fig. 7a and are, therefore, omitted). This is consistent with findings in Mellage *et al.* (2018b), who suggested that the discrepancy could be due to the metabolic dependence of parameters such as CEC_B and $\beta_{(+)}$, which do not remain constant. The discrepancy suggests that parameters controlling the mobility of ions tangential to cell membranes remain poorly constrained, and that contributions of mechanisms such as diffuse-layer polarization should perhaps be considered (Lyklema, Dukhin and Shilov, 1983).

3.4 NO$_2^-$ induced relaxation time anomalies

Cell size, determined via a flow cytometry non-fluorescent microbead calibration, remained relatively unchanged, between 1.4 and 1.6 μm, throughout the experiment (Fig. 4d). Despite the relatively constant cell size, the τ exhibited two distinct anomalies (Fig. 4d). At 13 hours, τ increased to 0.3 seconds from a stable 0.08 seconds during phase I. During phase II, it gradually decreased over 40 hours and levelled off at 0.05 seconds after 53 hours, and remained relatively constant until phase IV. A second anomaly was measured in phase IV. At the same time as the peak-σ'' dropped (Fig. 4c), τ increased from 0.06 to 0.3 s. Concurrent to the σ'' rebound, τ gradually decreased at 220 hours to level off at around 0.05 seconds at 253 hours.

Both anomalies in τ matched the timing of NO$_2^-$ accumulation in excess of 0.5 mM. Nitrite is known to have toxic effects on *S. oneidensis* (Zhang *et al.* 2013). It has also been shown that NO$_2^-$ can act as a protonophore (Sijbesma *et al.* 1996), a compound that decouples microbial catabolism from anabolism (hence inhibiting cell growth) by inducing drastic changes in the chemistry (e.g. pH changes) at or in direct proximity of the cell membrane (Saini 2014).

The presence of cells throughout the incubation and their relatively constant cell size suggests that the anomalies in τ are not a function of changes in cell size, but of changes in the surface charging properties of the cells in response to NO$_2^-$ induced stress (Soni *et al.* 2008). We speculate that two parallel mechanisms drive the increase in τ. The first mechanism is related to the localized build-up of protons at the outer cell membrane during uncoupling, which decreases pH, resulting in a localized reduction in negatively charged sites (Saini 2014). As an added line of evidence, we compare σ' variations with τ dynamics, specifically during the second, most pronounced τ anomaly, in Fig. 8. The comparison in Fig. 8 highlights that τ anomalies are coincident with sharp increases in σ' (followed by a small gradual increase until the
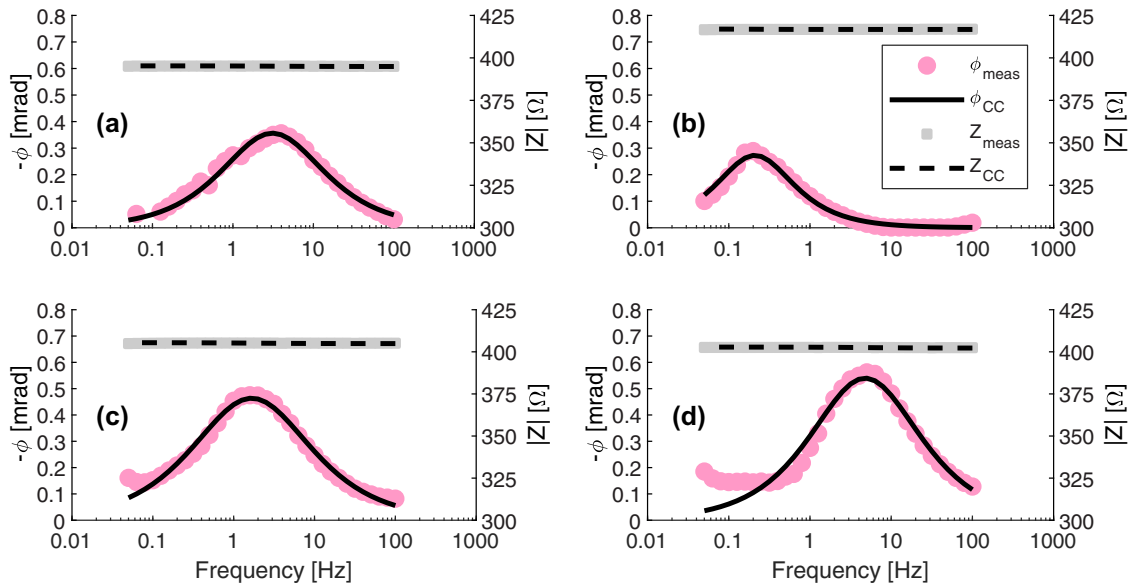
Figure 6 Fit of a single Cole–Cole relaxation to phase (φ) and impedance (Z) data in column G2 at (a) 81, (b) 195, (c) 246 and (d) 280 hours.

end of each no-flow phase), suggesting a change in the surface charge density of the cells, which alters aqueous and sorbed concentrations of cations. For example, an increase in τ would suggest a decrease in ion mobility, perhaps related to the lower prevalence of negatively charged sites, resulting in a release of EDL-bound cations from the cell membrane. These findings support those of Mellage *et al.* (2018b), where τ dynamics were linked to changes in the metabolic state of *S. oneidensis* cells. Furthermore, nitrite toxicity can lead to enhanced cell lysis, which results in the production of extracellular DNA (eDNA; Gödeke *et al.* 2011; Das, Sehar and Manefield 2013; Turnbull *et al.* 2016). Rosier *et al.* (2019) measured a decrease in the σ'' of *P. aeruginosa* cells with the addition of increasing concentrations of eDNA. At the outer cell membrane, eDNA can chelate mobile cations (Mulcahy *et al.* 2008), reducing ion

mobility, acting as a second mechanism occurring in parallel, driving the measured increase in the relaxation time, during both τ anomalies. (Note: We discount changes in pH as a potential factor influencing the background polarization of the quartz sand, because the experiment was buffered (pH 7.5). Furthermore, Skold, Revil and Vaudelet (2011) showed that variations in the neutral pH-range do not significantly affect the σ'' of quartz sand.)

3.5 Cell surface diffusion coefficient

Relying on the relatively constant trend in cell size, the average cell size for the period after the anomaly in τ and before the second injection (phase III) of 1.45 µm (within the range of widths and lengths reported for *S. oneidensis,* 1–5 µm;
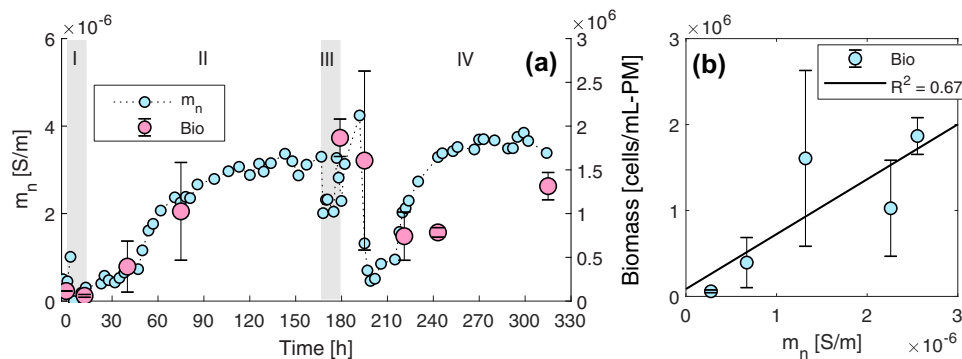

Figure 7 Normalized chargeability (m_n) and measured biomass density (Bio), as a function of time (a), and a linear relationship between m_n measured cell counts (FACS) ($R^2 = 0.67$) prior to the precipitous decline in m_n at 195 hours (b).
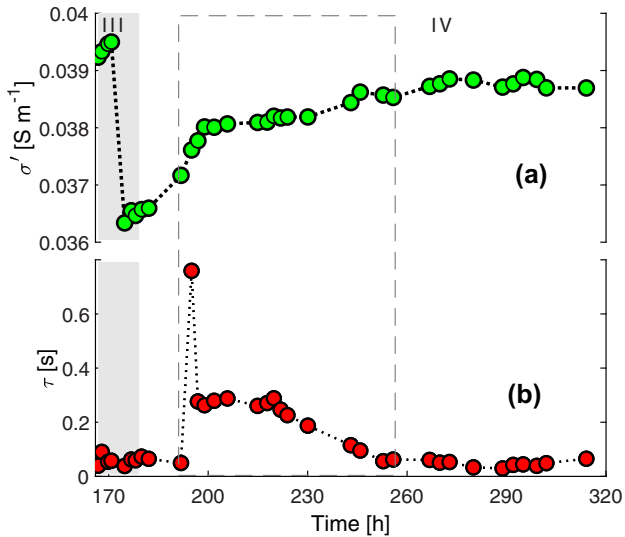
Figure 8 Comparison between real conductivity (σ') and relaxation time (τ), zoomed-in view during phases III and IV (a and b), highlighting the more pronounced increase in σ' during the second τ anomaly.

Lee *et al.* 2016) was used to compute an apparent surface diffusion coefficient (Kruschwitz *et al.* 2010), for *S. oneidensis*, by rearranging equation (4). During the period between 35 and 167 hours, the calculated D_s for the polarizing bacteria is 5.4 (± 1.3) $\mu m^2\ s^{-1}$. It is noteworthy that the cell size estimation is only an indirect measure of cell size as a function of light scatter, which can also be affected by changing cell physiology, highlighting the inherent uncertainty in the estimation of effective cell diameters (Vives-Rego, Lebaron and Nebe-von Caron 2000). Nevertheless, the value of D_s reported here is within the range of values for D_s computed from Revil *et al.* (2012): 0.44 to 14 $\mu m^2\ s^{-1}$, using ion mobility coefficients reported therein (1.7–$5.5 \times 10^{-10}\ m^2\ s^{-1}\ V^{-1}$), for various cell strains, and similar to D_s proposed for clay minerals (3.8 $\mu m^2\ s^{-1}$; Revil 2013), which have ionic mobility coefficients similar to bacterial cells (Revil *et al.* 2012; Zhang *et al.* 2014). To our knowledge, this is the first reported estimate of a Stern layer ionic diffusion coefficient computed directly from measurements of the effective diameter of polarizing bacterial cells. The estimated D_s reported here, for *S. oneidensis* cells, may also be used to extract qualitative information of cell size from the peak relaxation of SIP data sets.

4 CONCLUSION

The strong dependence of σ'' (and m_n) on biomass density in porous media, highlighted herein, supports its applicability

as a tool for estimating bacterial concentrations in natural porous media. Measured anomalies in τ corresponding to peak NO_2^- accumulation are evidence for the changing surface diffusion characteristics of cell membranes in response to NO_2^- induced stress (toxic effects and uncoupling) and, additionally, highlight that spectral induced polarization (SIP) can be used as a qualitative tool to infer changes in microbial activity. The potential for development of a cell size calibration with SIP would greatly benefit from targeted experiments to monitor mixed microbial communities (e.g. two or more strains of distinct sizes), as opposed to pure cultures. Nonetheless, our analysis of the response of σ'' to microbial growth provides a theoretical framework from which to build upon using bench-scale experiments of increasing complexity, leading to the eventual field scale SIP deployment.

REFERENCES

Abdel Aal G.Z., Atekwana E.A. and Atekwana E.A. 2010. Effect of bioclogging in porous media on complex conductivity signatures. *Journal of Geophysical Research: Biogeosciences* **115**, G00G07.

Archie G.E. 1942. The electrical resistivity log as an aid in determining some reservoir characteristics. *Transactions of the AIME.* **146**, 54–62.

Bastida F., Kandeler E., Moreno J., Ros M., García C. and Hernández T. 2008. Application of fresh and composted organic wastes modifies structure, size and activity of soil microbial community under semiarid climate. *Applied Soil Ecology* **40**, 318–329.

Ceazan M.L., Thurman E.M. and Smith R.L. 1989. Retardation of ammonium and potassium transport through a contaminated sand and gravel aquifer: the role of cation exchange. *Environmental Science and Technology* **23**, 1402–1408.

Chubar N., Behrends T. and Van Cappellen P. 2008. Biosorption of metals (Cu2+, Zn2+) and anions (F−, H2PO4−) by viable and autoclaved cells of the Gram-negative bacterium *Shewanella putrefaciens*. *Colloids and Surfaces B: Biointerfaces* **65**, 126–133.

Claessens J., Behrends T. and Van Cappellen P. 2004. What do acid-base titrations of live bacteria tell us? A preliminary assessment. *Aquatic Sciences* **66**, 19–26.

Cox J.S., Smith D.S., Warren L.A. and Ferris F.G. 1999. Characterizing heterogeneous bacterial surface functional groups using discrete affinity spectra for proton binding. *Environmental Science and Technology* **33**, 4514–4521.

Das T., Sehar S. and Manefield M. 2013. The roles of extracellular DNA in the structural integrity of extracellular polymeric substance and bacterial biofilm development. *Environmental Microbiology Reports* 5, 778–786.

Davis C.A., Atekwana E., Atekwana E., Slater L.D., Rossbach S. and Mormile M.R. 2006. Microbial growth and biofilm formation in geologic media is detected with complex conductivity measurements. *Geophysical Research Letters* 33, L18403.

Gao H., Yang Z.K., Barua S., Reed S.B., Romine M.F., Nealson K.H., *et al.* 2009. Reduction of nitrate in *Shewanella oneidensis* depends on atypical NAP and NRF systems with NapB as a preferred electron transport protein from CymA to NapA. *ISME Journal* 3, 966–976.

Gödeke J., Paul K., Lassak J. and Thormann K.M. 2011. Phage-induced lysis enhances biofilm formation in *Shewanella oneidensis* MR-1. *ISME Journal* 5, 613.

Kemna A., Binley A., Cassiani G., Niederleithinger E., Revil A., Slater L., *et al.* 2012. An overview of the spectral induced polarization method for near-surface applications. *Near Surface Geophysics* 10, 453–468.

Kruschwitz S., Binley A., Lesmes D. and Elshenawy A. 2010. Textural controls on low-frequency electrical spectra of porous media. *Geophysics* 75, WA113–WA123.

Lee C.K., Kim A.J., Santos G.S., Lai P.Y., Lee S.Y., Qiao D.F., *et al.* 2016. Evolution of cell size homeostasis and growth rate diversity during initial surface colonization of *Shewanella oneidensis*. *ACS Nano.* 10, 9183–9192.

Lyklema J., Dukhin S. and Shilov V. 1983. The relaxation of the double layer around colloidal particles and the low-frequency dielectric dispersion: part I. Theoretical considerations. *Journal of Electroanalytical Chemistry and Interfacial Electrochemistry* 143, 1–21.

Mellage A., Holmes A.B., Linley S., Vallée L., Rezanezhad F., Thomson N., *et al.* 2018a. Sensing coated iron-oxide nanoparticles with spectral induced polarization (SIP): experiments in natural sand packed flow-through columns. *Environmental Science and Technology* 52, 14256–14265.

Mellage A., Smeaton C.M., Furman A., Atekwana E.A., Rezanezhad F. and Van Cappellen P. 2018b. Linking spectral induced polarization (SIP) and subsurface microbial processes: Results from sand column incubation experiments. *Environmental Science and Technology* 52, 2081–2090.

Mulcahy H., Charron-Mazenod L. and Lewenza S. 2008. Extracellular DNA chelates cations and induces antibiotic resistance in Pseudomonas aeruginosa biofilms. *PLoS Pathogens* 4, e1000213.

Neal A.L., Rosso K.M., Geesey G.G., Gorby Y.A. and Little B.J. 2003. Surface structure effects on direct reduction of iron oxides by *Shewanella oneidensis*. *Geochimica et Cosmochimica Acta* 7, 4489–4503.

Pelton W., Ward S., Hallof P., Sill W. and Nelson P.H. 1978. Mineral discrimination and removal of inductive coupling with multifrequency IP. *Geophysics* 43, 588–609.

Revil A. 2013. Effective conductivity and permittivity of unsaturated porous materials in the frequency range 1 mHz–1 GHz. *Water Resources Research* 49, 306–327.

Revil A., Atekwana E., Zhang C., Jardani A. and Smith S. 2012. A new model for the spectral induced polarization signature of bacterial growth in porous media. *Water Resources Research* 48, W09545.

Ringuet S., Sassano L. and Johnson Z.I. 2011. A suite of microplate reader-based colorimetric methods to quantify ammonium, nitrate, orthophosphate and silicate concentrations for aquatic nutrient monitoring. *Journal of Environmental Monitoring* 13, 370–376.

Rosier C.L., Atekwana E.A., Aal G.A. and Patrauchan M.A. 2019. Cell concentrations and metabolites enhance the SIP response to biofilm matrix components. *Journal of Applied Geophysics* 160, 183–194.

Russell J.B. and Cook G.M. 1995. Energetics of bacterial growth: balance of anabolic and catabolic reactions. *Microbiological Reviews* 59, 48–62.

Saini G. 2014. Metabolic uncoupling: biomass control strategy in microbial processes. *Journal of Microbial and Biochemical Technology* 6, e117.

Schwarz G. 1962. A theory of the low-frequency dielectric dispersion of colloidal particles in electrolyte solution1, 2. *The Journal of Physical Chemistry* 66, 2636–2642.

Seeliger S., Janssen P.H. and Schink B. 2002. Energetics and kinetics of lactate fermentation to acetate and propionate via methylmalonyl-CoA or acrylyl-CoA. *FEMS Microbiology Letters* 211, 65–70.

Sijbesma W.F., Almeida J.S., Reis M.A. and Santos H. 1996. Uncoupling effect of nitrite during denitrification by *Pseudomonas fluorescens*: an in vivo 31P-NMR study. *Biotechnology and Bioengineering* 52, 176–182.

Simunek J., Van Genuchten M.T. and Sejna M. 2005. The HYDRUS-1D software package for simulating the one-dimensional movement of water, heat, and multiple solutes in variably-saturated media. *University of California-Riverside Research Reports* 3, 1–240.

Skold M., Revil A. and Vaudelet P. 2011. The pH dependence of spectral induced polarization of silica sands: Experiment and modeling. *Geophysical Research Letters* 38, L12304.

Sokolov I., Smith D., Henderson G., Gorby Y. and Ferris F. 2001. Cell surface electrochemical heterogeneity of the Fe (III)-reducing bacteria *Shewanella putrefaciens*. *Environmental Science and Technology* 35, 341–347.

Soni K.A., Balasubramanian A.K., Beskok A. and Pillai S.D. 2008. Zeta potential of selected bacteria in drinking water when dead, starved, or exposed to minimal and rich culture media. *Current Microbiology* 56, 93–97.

Turnbull L., Toyofuku M., Hynen A.L., Kurosawa M., Pessi G., Petty N.K., *et al.* 2016. Explosive cell lysis as a mechanism for the biogenesis of bacterial membrane vesicles and biofilms. *Nature Communications* 7, 11220.

Vives-Rego J., Lebaron P. and Nebe-von Caron G. 2000. Current and future applications of flow cytometry in aquatic microbiology. *FEMS Microbiology Reviews* 24, 429–448.

Weigand M. and Kemna A. 2016a. Debye decomposition of time-lapse spectral induced polarisation data. *Computers and Geosciences* 86, 34–45.

Weigand M. and Kemna A. 2016b. Relationship between Cole–Cole model parameters and spectral decomposition parameters derived from SIP data. *Geophysical Journal International* 205, 1414–1419.

Zhang C., Revil A., Fujita Y., Munakata-Marr J. and Redden G. 2014. Quadrature conductivity: a quantitative indicator of bacterial abundance in porous media. *Geophysics* **79**, D363–D375.

Zhang H., Fu H., Wang J., Sun L., Jiang Y., Zhang L. *et al*. 2013. Impacts of nitrate and nitrite on physiology of *Shewanella oneidensis*. *Plos One* **8**, e62629.

SUPPORTING INFORMATION

Additional supporting information may be found online in the Supporting Information section at the end of the article.

Figure S1. Flow cytometry non-fluorescent microbead size calibration (F-13838 size calibration kit, Thermo Fisher) used to estimate the size of unstained, unfixed *S. oneidensis* cells.

Figure S2. Spectral imaginary conductivity comparison between columns G1 and G2 10 hours prior to and shortly after the first injection.

Figure S3. Imaginary conductivity, normalized for the maximum measured in each column (σ''_{norm}) for both SIP measurement columns, G1 and G2.

Figure S4. Lactate and acetate concentration time series.

Figure S5. Adenosine triphosphate (ATP) concentrations measured in the sacrificially sampled reactors.

Figure S6. Complex conductivity response of SIP column G2 of the growth incubation experiments undergoing two injections of nitrate and lactate compared with the response of a non-growth (NG) control column devoid of electron acceptor and electron donor.